Magnetically-induced CO_2 methanation using exchange – coupled spinel ferrites in cuboctahedron-shaped nanocrystals

Beatriz Rivas-Murias,*[a] Juan M. Asensio,*[b] Nicolas Mille,[b] Benito Rodríguez-González,[c] Pier-Francesco Fazzini,[b] Julian Carrey,[b] Bruno Chaudret,*[b] Verónica Salgueiriño*[a]

[a] Dr. Beatriz Rivas-Murias, Dr. Verónica Salgueiriño
Departamento de Física Aplicada and CINBIO
Universidade de Vigo, 36310, Vigo (Spain)
E-mail: brivas@uvigo.es; vsalgue@uvigo.es

[b] Dr. Juan M. Asensio, Dr. Nicolas Mille, Dr. Pier-Francesco Fazzini, Dr. Julian Carrey, Dr. Bruno Chaudret
Laboratoire de Physique et Chimie des Nano-Objets (LPCNO)
Université de Toulouse, CNRS, INSA, UPS, 135 avenue de Rangueil, 31077 Toulouse (France)
E-mail: asensior@insa-toulouse.fr; chaudret@insa-toulouse.fr

[c] Dr. Benito Rodríguez-González
CACTI, Universidade de Vigo, 36310, Vigo (Spain)

Abstract: A magnetically induced catalysis can be promoted taking advantage of optimal heating properties from the magnetic nanoparticles to be employed. However, if unprotected, these heating agents that are usually air-sensitive, get sintered under the harsh catalytic conditions. In this context, we present, to the best of our knowledge, the first example of air-stable magnetic nanoparticles that: a) show an excellent performance as heating agents in the CO_2 methanation catalyzed by Ni/SiRAlOx, with CH_4 yields above 95%, and b) do not sinter under reaction conditions. To attain both characteristics we demonstrate, first the exchange-coupled magnetic approach as an alternative and effective way to tune the magnetic response and heating efficiency, and second, the chemical stability of cuboctahedron-shaped core-shell hard $CoFe_2O_4$ - soft Fe_3O_4 nanoparticles.

Magnetically-induced catalysis is based on the heat generated by magnetic nanoparticles (NPs) when exposed to an alternating magnetic field.[1–3] Recently, it has been demonstrated that this approach can be used to perform heterogeneous reactions at high temperature, such as CO_2 hydrogenation, using $Fe_{2.2}C$ NPs as heating agents and Ni or Ru NPs supported on SiRAlOx as catalysts,[3–5] or by using bimetallic FeNi alloys as both heating agent and catalyst.[6] However, one important limitation of these metallic heating agents is that they are prone to oxidation, so that, they must be handled under inert atmosphere to preserve their heating capacities. Additionally, these materials sinter under the harsh reaction conditions (above 320-400 ºC), which depletes their heating performances, hindering consequently their recyclability. To overcome these issues, magnetic transition metal oxide NPs are promising alternative systems, which are cheap, abundant and stable against oxidation. However, in general, metallic oxides are soft magnets that usually display low values of heating power at the operating conditions. One attractive option to harden but also to increase the magnetization of these materials in order to improve their heating power is to utilize conventional hard/soft or inverted soft/hard core-shell metallic oxide heterostructures. This way makes possible to utilize hard oxides upon taking advantage of the exchange anisotropy at the interface between the core and the shell, which can be optimized by increasing the thickness (or the volume fraction in the case of NPs) of the soft

phase[7]. Increasing the thickness can even force the transition from a rigidly exchange-coupled to an exchange-spring behavior,[8–12] modifying the magnetic response and magnetization, and consequently, the heat release capacity.

The heating power is quantified in terms of the specific absorption rate (SAR) in $W \cdot g^{-1}$, which expresses the amount of energy released (in general equal to the energy absorbed) by the material as a function of time. The heating power in the presence of an alternating magnetic field[13],[14] stems mainly from hysteresis losses[15],[16]. Accordingly, we can take advantage of this magnetic heating, directly and homogeneously distributed within the catalyst, without the need for heating the whole reactor. In addition, this magnetically-induced catalysis allows the system to reach the reaction temperatures in a few seconds.

A potential field of application of this methodology, as above mentioned, is CO_2 hydrogenation, the so-called Sabatier reaction ($CO_{2(g)} + 4H_{2(g)} \leftrightarrow CH_{4(g)} + 2H_2O_{(g)}$).[17],[18] Thus, given the notable hazardous increase of the atmospheric CO_2 concentration[19] and the requirement for renewable resources, a very convenient solution to mitigate these continuous CO_2 emissions is to use it as a platform molecule towards high value products and fuels. However, the high kinetic energy barrier required for the activation of the CO_2 molecule forces the use of relatively harsh reaction conditions (temperatures above 300 ºC).[20–22]

With the aforementioned into account, the present work focuses on the synthesis of $Co_{0.6}Fe_{2.4}O_4$ (**CFO**) and of core-shell $Co_{0.6}Fe_{2.4}O_4$-Fe_3O_4 (**CFO@FO**) cuboctahedron-shaped NPs. The samples are characterized in terms of crystalline structure, magnetic properties under static and dynamic magnetic fields, and heating efficiency, as a function of the magnetite shell thickness. Furthermore, their high performance as heating agents in the magnetically-induced catalyzed CO_2 methanation is proven.

Cuboctahedron-shaped cobalt ferrite NPs were synthesized by thermal decomposition of $Co(acac)_2$ and $Fe(acac)_3$ in the presence of a mixture of oleic and stearic acid, mmol ratio of 2:0.9. The geometric mean of the particle size was 95.1 */ 1.5 nm (using a log-normal distribution, where the larger dimension and a 95.5% interval of confidence were considered for the size distribution analysis, see Figures 1a and 1b)[23]. Figure 1a shows a Transmission Electron Microscopy (TEM) image of a group of these **CFO** NPs evidencing their cuboctahedral shape and the formation of chains, as a result of dipolar interactions among particles. The X-Ray diffraction (XRD) pattern of this sample (Figure 1c) shows that these NPs crystallize in the typical cubic spinel structure (*Fd-3m* symmetry group), with a lattice parameter of 0.8392 nm.[24–26] The average crystallite size in the **CFO** NPs is around 43-45 nm, obtained using the Scherrer formula[27]. This range corresponds to approximately the half of the grain sizes obtained by TEM. The average composition of the sample, studied by Electron Dispersive X-Ray Spectroscopy (EDS) analysis in several particles, indicates an average Co:Fe ratio of 1:3.7, resulting in an empirical formula of $Co_{0.64(1)}Fe_{2.36(1)}O_4$ (Figure S1 in the Supporting information, SI).

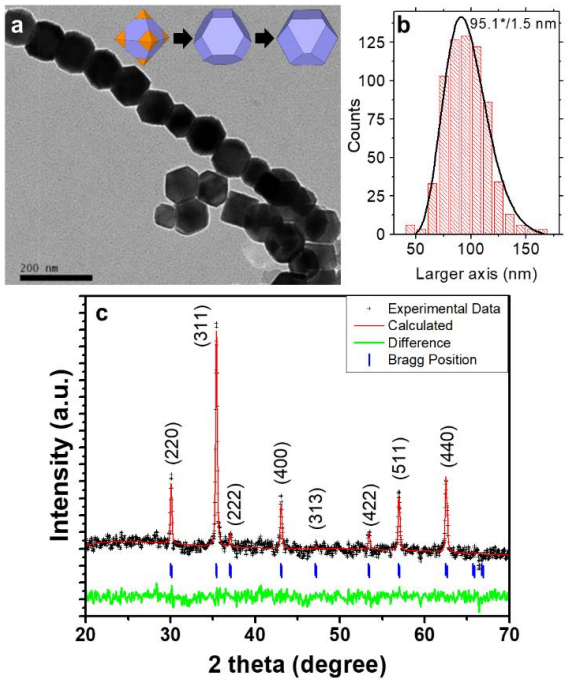

Figure 1. TEM image (a), size distribution histogram centered at 95.1 */ 1.2 nm considering the larger dimension of the nanocrystal and fitted to a log-normal curve (b) and X-Ray powder diffraction pattern with Rietveld refinement of the cuboctahedron-shaped $Co_{0.6}Fe_{2.4}O_4$ nanocrystals (c). Inset (a): scheme of the construction of a regular and irregular truncated octahedron from an octahedral shape.

The crystalline structure and morphology of the particles were also studied by High-Resolution TEM (HRTEM). Figure S2a (in the SI) displays a HRTEM image of an isolated **CFO** particle, on which a twin dividing the nanocrystal in two equal parts is observed. From this image, crystalline domains of ~47 nm along the twinned defect, confirm the values of average crystallite size obtained in the XRD analysis. Figure S2b shows a higher resolution image of this kind of twinned defect, where both halves of the crystal display parallel crystallographic planes. Furthermore, the selected area electron diffraction (SAED) pattern of this isolated **CFO** nanocrystal is shown in Figure S2c and corroborates the highly crystalline spinel structure. Additionally, elemental mappings of iron, cobalt and oxygen of the isolated nanocrystal are shown in Figure S2d.

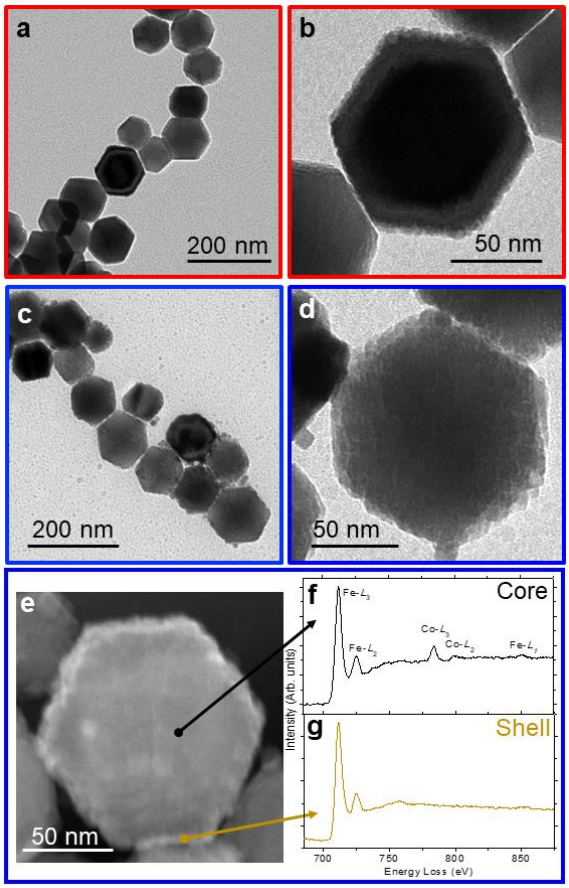

Figure 2. Low and high magnification TEM images of cobalt ferrite nanocrystals with thinner (CFO@FO1, in red, a and b) and thicker (CFO@FO3 in blue, c and d) magnetite shells. HAADF-STEM image of an isolated particle from the sample with thicker magnetite shell (CFO@FO3 in blue, e) and EELS spectra recorded from the particle core (f) and shell (g).

The magnetic response of these $Co_{0.6}Fe_{2.4}O_4$ truncated octahedra can be modified by means of the exchange-spring magnetic approach,[8–12] taking advantage of an additional soft magnetic shell. This shell, rigidly exchange-coupled, increases magnetization while keeping high coercivity, parameters involved in the heat released capacity to be improved. In this case, in order to study the exchange coupling effect, a shell of the magnetite (Fe_3O_4, **FO**) soft phase was grown onto the $Co_{0.6}Fe_{2.4}O_4$ hard phase working as core. Samples of the cuboctahedron-shaped cobalt ferrite NPs coated with a magnetite shell of different thickness (1.5, 4 and ~8.5 nm, denoted as **CFO@FO1**, **CFO@FO2** and **CFO@FO3**, respectively) were therefore prepared. TEM images of these core-shell nanostructures, with the thinnest (**CFO@FO1**) and the thickest (**CFO@FO3**) magnetite shell, are shown in Figures 2a-d. The higher magnification images on the right show individual nanostructures with a much rougher surface, if compared with the initial vey flat surface facets of the single truncated octahedra. The two phases located either at the core or at the shell show the same spinel structure with a slight lattice mismatch between them, which implies consequently the plane distribution in the [111] direction in both phases to be epitaxial, as displayed in Figure S3. The electron

energy loss spectroscopy (EELS) analysis was performed in these samples (Figures 2f-g, and Figure S4), showing that, while Fe peaks (Fe-$L_{2,3}$ at 712 (L_3) and 725 eV (L_2); Fe-L_1 at 846 eV) were detected both at the core and the shell of the NPs, the presence of Co (Co-$L_{2,3}$ at 785 (L_3) and 800 eV (L_2)) was only detected at the core.[28] The absence of a pre-peak in the Fe-$L_{2,3}$ edges, which has been reported as indication of a change in the iron valence to more oxidized compounds, such as hematite,[29],[30] implies the presence of magnetite as the single iron oxide phase in the studied samples. In line with this, no other iron oxides were detected by Raman spectroscopy (see Figure S5 in the SI).

Furthermore, to prove the exchange-coupling at the interface between the two magnetic phases present in the core-shell NPs, hysteresis loops of these systems were studied at 10 K (Figure 3) and 300 K (Figure S7). The initial **CFO** sample shows a single-step hysteresis loop at these temperatures, with values of maximum magnetization of ~78 A m^2 kg^{-1} and ~72 A m^2 kg^{-1}, and values of coercive field ($\mu_0 H_C$) of ~690 mT and ~ 100 mT, respectively. Both values are in the same range as previously reported for $Co_{0.6}Fe_{2.4}O_4$ NPs with smaller sizes.[31],[32] Hysteresis loops of the core-shell nanostructures synthesized, with the thinnest (**CFO@FO1**, in red) and the thickest (**CFO@FO3**, in blue) magnetite shell are shown in Figure 3. Table 1 summarizes the magnetic properties of the four samples considered, offering a progressive increase in the maximum magnetization and decrease in the coercive field, upon increasing the thickness of the magnetite soft shell.

Table 1. Values of the coercive field and maximum magnetization at 10 K and 300 K for the $Co_{0.64}Fe_{2.36}O_4$ samples as increasing the Fe_3O_4 shell thickness.

Samples	$\mu_0 H_c$ (mT)		M_{max} (A m^2 kg^{-1})		Fe_3O_4 thickness (nm)
	10 K	300 K	10 K	300 K	
CFO	689.4	105.0	78.0	71.6	-
CFO@FO1	675.8	73.8	84.7	78.5	1.5
CFO@FO2	511.9	75.2	93.4	86.7	4.0
CFO@FO3	421.3	72.6	94.2	86.9	8.5

As mentioned, the magnetic coupling at the interface between the core and shell can induce a transition from a rigidly exchange-coupled (with a characteristic single-hysteresis loop and an averaged M_{max} and $\mu_0 H_C$) to an exchange-spring (with a characteristic two-step magnetic hysteresis loop) behavior, as increasing the soft layer thickness.[8],[9] Since the critical soft layer thickness for $Co_{0.6}Fe_{2.4}O_4$ sample is ~ 15 nm (see comment S8 in the SI), and the studied systems are below this critical value, an exchange-coupled behavior is therefore favored. The fact of having M_{max} and $\square_0 H_C$ values between those characteristic of the isolated **FO** and **CFO** phases points indeed to the magnetic exchange-coupled scenario,[9],[11] implying as well the sharp interface stemming from the very flat surface facets of the cuboctahedra in the final core-shell heterostructures. The characteristic single-hysteresis loops also exclude effects related to cationic interdiffusion at the interface. To further confirm

this issue, we have additionally compared the experimentally registered and theoretically calculated reversal field ($\mu_0 H_{SW}$) values (see comment S9 and Figure S10), obtaining a good agreement.

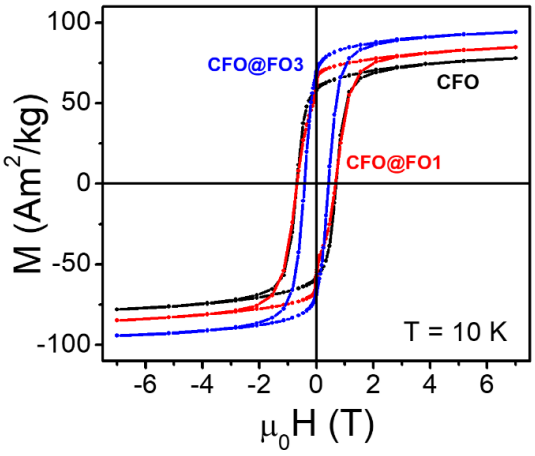

Figure 3. Field dependent magnetization plots measured at 10 K of the **CFO** (in black), **CFO@FO1** (in red) and **CFO@FO3** (in blue).

The heating properties of **CFO** and **CFO@FO1-3** samples under alternating field were first studied by calorimetry[4] at a frequency of 93 kHz and at room temperature (Figure 4a). While the SAR values for **CFO**, **CFO@FO1** and **CFO@FO3** samples at $\mu_0 H_{rms}$ = 47 mT are in the 150-185 W·g^{-1} range, the best performance is obtained for **CFO@FO2** sample, with a SAR value of *ca*. 270 W·g^{-1}. Interestingly, the onset field value decreases as the Fe_3O_4 shell thickness increases. Indeed, the introduction of the soft magnetic material reduces the coercive field of the NPs favoring their reversal to get significant hysteresis losses at lower field amplitudes.

The heating properties of these systems were also studied through high-frequency hysteresis loop measurements at room temperature.[15] Hysteresis loops applying a frequency of 50 kHz and an amplitude magnetic field of $\mu_0 H_{rms}$ = 55 mT were measured (see Figure 4b). While samples **CFO** and **CFO@FO1** display low-susceptibility and slightly opened hysteresis loops ($\mu_0 H_C$ ~4.8 and 5.7 mT, respectively), both the susceptibility and $\mu_0 H_C$ and M_{max} values notably increase for the samples with the thickest Fe_3O_4 shells ($\mu_0 H_C$ ~16.8 and ~12.6 mT and M_{max} *ca*. 18 and 15 A·m^2·kg^{-1} for **CFO@FO2** and **CFO@FO3**, respectively). In these conditions, the SAR values obtained by high-frequency magnetometry are 1.80, 2.76, 48.7 and 34.3 W·g^{-1} for **CFO**, **CFO@FO1**, **CFO@FO2** and **CFO@FO3**, respectively. The highest value was observed for **CFO@FO2** in agreement with calorimetric measurements. We attribute the observed differences between the normalized SAR values determined by magnetometry and those obtained by calorimetry to the different frequencies used for each method. Thus, at 50 kHz, higher field amplitudes would be required to activate the less-heating samples **CFO** and **CFO@FO1**, explaining their very low SAR determined by magnetometry.

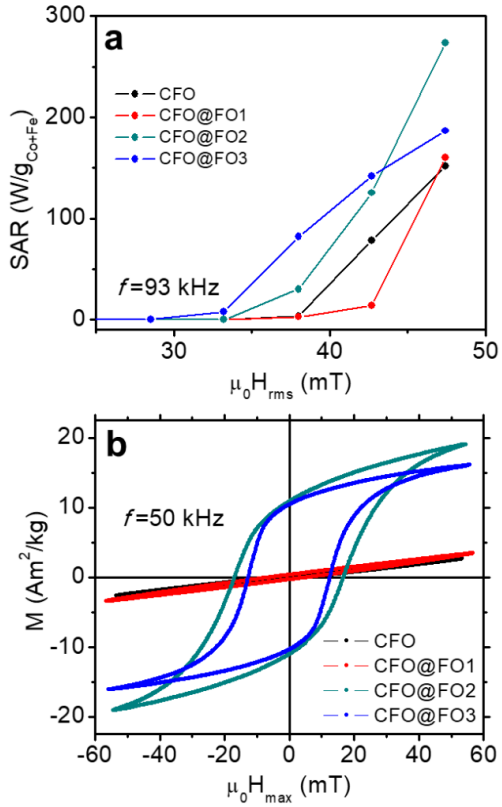

Figure 4. SAR values measured by calorimetry at a frequency of 93 kHz (a) and high-frequency hysteresis loops at 50 kHz (b) at room temperature for the $Co_{0.6}Fe_{2.4}O_4$ samples with different Fe_3O_4 shell thickness.

Finally, the viability of **CFO** and **CFO@FO2** as heating agents in magnetically-induced CO_2 methanation catalyzed by Ni/SiRAlOx was evaluated (see Figure 5). For that, **CFO** and **CFO@FO2** were first mixed with Ni/SiRAlOx (see experimental section and Figure S11 in the SI for details), such that **CFO/Ni/S** and **CFO@FO2/Ni/S** catalytic systems, respectively, were attained. The metal content of both systems was determined by inductively coupled plasma-atomic emission spectroscopy (ICP-AES), obtaining 1.2 wt% of Co, 4.5 wt% of Fe and 8.0 wt% of Ni for **CFO/Ni/S**, and 0.7 wt% of Co, 3.5 wt% of Fe and 7.1 wt% of Ni for **CFO@FO2/Ni/S**. The catalytic reactions were performed in a glass flow reactor using an up-flow H_2/CO_2 molar ratio of 4 and 400 mg of catalyst under atmospheric pressure and with a total flow rate of 25 $mL \cdot min^{-1}$ (46.9 $L \cdot h^{-1} \cdot g_{(Ni)}^{-1}$ for **CFO/Ni/S** and 52.8 $L \cdot h^{-1} \cdot g_{(Ni)}^{-1}$ for **CFO@FO2/Ni/S**). The products obtained from the catalyzed reactions were monitored by gas chromatography (Figure S12).

In both cases, the selectivity toward CH_4 formation is of 100%. The highest performances of both catalysts (>95% CO_2 conversion) are reached when applying 53 mT, with global temperatures of *ca.* 450ºC (**CFO/Ni/S)** and *ca.* 400ºC (**CFO@FO2/Ni/S)**. Interestingly, despite their higher SAR and lower coercive field, **CFO@FO2** heterostructures were the heating agents that required higher magnetic field amplitudes to activate the catalytic reaction. Nevertheless, this fact can be related to the lower amount of heating agent in the

final catalyst employed (5.7 wt% of Co+Fe in **CFO/Ni/S** vs. 4.2 wt% of Co+Fe in **CFO@FO2/Ni/S**). As the coercive field decreases with temperature, another likely explanation is that during the experiment, the **CFO** NPs display a larger $\mu_0 H_C$ at high temperatures than that of **CFO@FO2** NPs. This stems from the fact that because of the heat release itself, higher magnetic field amplitudes are required to achieve the best performances in the latter case.

Importantly, both catalytic systems show good stability, with reaction profiles which could be reproduced once the process is finished and after removal of the H_2O accumulated in the water trap. The samples were analyzed by STEM, performing EDX mappings before and after the catalytic reaction (Figure S13). While the Ni nanoparticles have undergone a sintering process, promoted by the high temperatures (ca. 400-420 ºC),[3] **CFO** and **CFO@FO2** NPs did not coalesce. Overall, these heating agents can therefore be considered as highly stable towards sintering after 8 hours on stream, even at the high temperatures reached in the catalyzed processes.

In conclusion, we demonstrate here that oxide nanoparticles can be also used as heating agents in magnetically induced catalysis thanks to their magnetic properties and their optimization using the exchange coupling between a soft and hard magnetic layer. Thus, core-shell nanoparticles, namely cuboctahedron-shaped $CoFe_2O_4$-Fe_3O_4 were synthesized, with a soft shell thickness ranging from 1.5 to 8.5 nm. The magnetic properties of these heterostructures were studied and analyzed in terms of the exchange-spring magnetic approach, by which the coating with a soft layer decreases the coercivity influencing consequently their heating properties. The system with a 4 nm thick magnetite shell shows the maximum SAR value of ~270 $W \cdot g^{-1}$ (at 47 mT and 93 kHz). The performance of these core-shell nanostructures as heating agents in the magnetically-favored CO_2 methanation catalyzed by Ni/SiRAlOx was therefore investigated, using the non-coated truncated octahedra as reference. Since both systems show high CO_2 conversions (above 95%), with a remarkable stability toward sintering at the reaction temperatures attained (ca. 400-440 ºC), these findings constitute a notable improvement in comparison to previous results reported. Furthermore, the air-stability and the easy external magnetic manipulation of these oxide nanoparticles render them promising heating agents for catalysis in aqueous solution such as biomass valorization.[33]

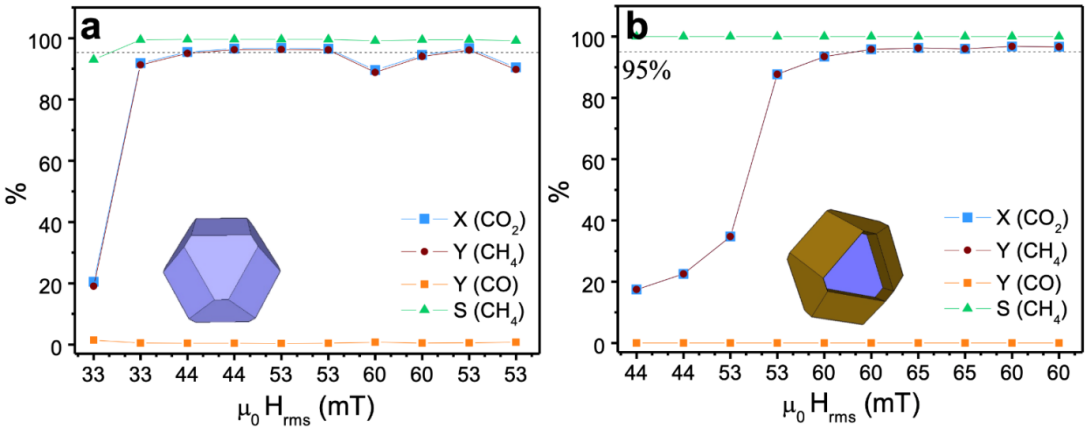

Figure 5. Percentage of CO_2 conversion, CH_4 and CO yields and CH_4 selectivity as a function of $\mu_0 H_{rms}$ for **CFO/Ni/S** (a) and for **CFO@FO2/Ni/S** systems (b). Sketches in blue and in blue-brown represent the single $Co_{0.6}Fe_{2.4}O_4$ phase and the core-shell $Co_{0.6}Fe_{2.4}O_4$@ Fe_3O_4 cuboctahedron employed for the heating, respectively. Dashed lines indicate the 95 % level.

Acknowledgements

The authors acknowledge the financial support from the Xunta de Galicia (IN607 A 2018/5 and ED431C 2016-034), the Spanish Ministerio de Economía y Competitividad (CTM2017-84050-R) and the ERC Advanced Grant (MONACAT 2015-694159).

Keywords: spinel ferrite • core-shell nanostructure • exchange-coupling • specific absorption rate • CO_2 methanation

Bibliography

[1] S. Ceylan, C. Friese, C. Lammel, K. Mazac, A. Kirschning, *Angew. Chem. Int. Ed.* **2008**, *47*, 8950–8953.

[2] S. Ceylan, L. Coutable, J. Wegner, A. Kirschning, *Chem. a Eur. J.* **2011**, *17*, 1884–1893.

[3] S. S. Kale, J. M. Asensio, M. Estrader, M. Werner, A. Bordet, P. Fazzini, D. Yi, J. Marbaix, K. Soulantica, B. Chaudret, *Catal. Sci. Technol.* **2019**, *9*, 2601–2607.

[4] A. Bordet, L. Lacroix, P. Fazzini, J. Carrey, K. Soulantica, B. Chaudret, *Angew. Chem. Int. Ed.* **2016**, *55*, 15894–15898.

[5] A. Bordet, M. Asensio, K. Soulantica, B. Chaudret, *Chem. Cat. Chem.* **2018**, *10*, 4047–4051.

[6] D. De Masi, J. M. Asensio, P.-F. Fazzini, L.-M. Lacroix, B. Chaudret, *Angew. Chemie Int. Ed.* **2020**, 1–6.

[7] R. Skomski, J. M. D. Coey, *Phys. Rev. B* **1993**, *48*, 15812–15816.

[8] E. F. Kneller, R. Hawig, *IEEE Trans. Magn.* **1991**, *27*, 3588–3600.

[9] E. E. Fullerton, J. S. Jiang, S. D. Bader, *J. Magn. Magn. Mater.* **1999**, *200*, 392–404.

[10] S. Yan, J. A. Barnard, F. Xu, J. L. Weston, G. Zangari, **2001**, *64*, 184403.

[11] A. López-Ortega, M. Estrader, G. Salazar-Alvarez, A. G. Roca, J. Nogués, *Phys. Rep.* **2015**, *553*, 1–32.

[12] G. Lavorato, E. Winkler, B. Rivas-Murias, F. Rivadulla, *Phys. Rev. B* **2016**, *94*, 054405.

[13] J. M. D. Coey, *Magnetism and Magnetic Materials*, Cambridge University Press, Cambridge, **2010**.

[14] Suriyanto, E. Y. K. Ng, S. D. Kumar, *Biomed. Eng. Online* **2017**, *16*, 36.

[15] Q. A. Pankhurst, J. Connolly, J. S. K., J. Dobson, *J. Phys. D-Applied Phys.* **2003**, *36*, R167–R181.

[16] B. Mehdaoui, A. Meffre, J. Carrey, S. Lachaize, L. M. Lacroix, M. Gougeon, B. Chaudret, M. Respaud, *Adv. Funct. Mater.* **2011**, *21*, 4573–4581.

[17] P. Sabatier, J. B. Senderens, *C. R. Hebd. Seances Acad. Sci.* **1902**, *134*, 514–516.

[18] P. Sabatier, J. B. Senderens, *C. R. Hebd. Seances Acad. Sci.* **1902**, *134*, 689–691.

[19] Hannah Ritchie and Max Roser, "CO_2 and Greenhouse Gas Emissions," can be found under https://ourworldindata.org/co2-and-other-greenhouse-gas-emissions, **n.d.**

[20] W. Wang, W. Shengping, X. M., J. Gong, *Chem. Soc.* **2011**, *40*, 3703–3727.

[21] J. Park, E. W. Mcfarland, *J. Catal.* **2009**, *266*, 92–97.

[22] J. Park, E. W. Mcfarland, *J. Catal.* **2011**, *279*, 403–404.

[23] E. Limpert, W. A. Stahel, M. Abbt, *Bioscience* **2001**, *51*, 341.

[24] G. Bate, in *Ferromagn. Mater.* (Ed.: E.P. Wohlfarth), North-Holland, Amsterdam, **1980**, p. 431.

[25] C. Pereira, A. M. Pereira, C. Fernandes, M. Rocha, R. Mendes, M. P. Fernández-García, A. Guedes, P. B. Tavares, J.-M. Grenèche, J. P. Araújo, et al., *Chem. Mater.* **2012**, *24*, 1496–1504.

[26] F. L. Deepak, M. Bañobre-López, E. Carbó-Argibay, M. F. Cerqueira, Y. Piñeiro-Redondo, J. Rivas, C. M. Thompson, S. Kamali, C. Rodríguez-Abreu, K. Kovnir, et al., *J. Phys. Chem. C* **2015**, *119*, 11947–11957.

[27] P. Scherrer, *Nachr Ges Wiss Goettingen* **1918**, 98–100.

[28] E. Bartolomé, P. Cayado, E. Solano, S. Ricart, J. Gázquez, B. Mundet, M. Coll, T. Puig, X. Obradors, M. Valvidares, et al., *New J. Chem.* **2016**, *40*, 6890–6898.

[29] T. P. Almeida, T. Kasama, A. R. Muxworthy, W. Williams, L. Nagy, T. W. Hansen, P. D. Brown, R. E. Dunin-Borkowski, *Nat. Commun.* **2014**, *5*, 1–6.

[30] S.-Y. Chen, A. Gloter, A. Zobelli, L. Wang, C.-H. Chen, C. Colliex, *Phys. Rev. B* **2009**, *79*, 1–10.

[31] Y. Yu, A. Mendoza-Garcia, B. Ning, S. Sun, *Adv. Mater.* **2013**, *25*, 3090–3094.

[32] A. Maher, M. Bakr, *J. Magn. Magn. Mater.* **2015**, *378*, 246–252.

[33] J. M. Asensio, A. B. Miguel, P. Fazzini, P. W. N. M. van Leeuwen, B. Chaudret, *Angew. Chemie* **2019**, 11428–11432.